Native and hydrogen-containing point defects in Mg_3N_2: A density functional theory study

Björn Lange, Christoph Freysoldt, and Jörg Neugebauer
Max-Planck-Institut für Eisenforschung GmbH, 40237 Düsseldorf, Germany
(Received 19 March 2010; revised manuscript received 31 May 2010; published 17 June 2010)

The formation energy and solubility of hydrogen in magnesium nitride bulk (antibixbyite Mg_3N_2) have been studied employing density functional theory in the generalized gradient approximation. The effect of doping and the presence of native defects and complex formation have been taken into account. Our results show that magnesium nitride is a nearly defect-free insulator with insignificant hydrogen-storage capacity. Based on this insight we derive a model that highlights the role of the formation and presence of the parasitic Mg_3N_2 inclusions in the activation of *p*-doped GaN in optoelectronic devices.

DOI: 10.1103/PhysRevB.81.224109 PACS number(s): 61.72.Bb, 61.72.J−, 61.72.sd, 61.72.uj

I. INTRODUCTION

The group-III nitrides *X*N (*X*=Al, Ga, In) and their alloys have evolved into the material class of choice for white light-emitting diodes (LEDs).[1,2] A major breakthrough in utilizing this material class was the discovery that *p*-type conductivity can be achieved in the originally fully hydrogen compensated or passivated material by thermal annealing in a hydrogen-free atmosphere. The common understanding is that Mg substituted on a metal site *X* is compensated or passivated by forming a neutral [MgH] complex.[2–5] During the activation process, the complex dissociates into the desired Mg acceptor and interstitial H^+, which readily diffuses, eventually forming H_2 molecules at the surface that can easily desorb.[4,6] However, the active dopant concentration that can be achieved with this process is limited by three effects. (1) At Mg concentrations above 3×10^{18} cm^{-3}, a parasitic Mg_3N_2 phase appears. In transmission electron micrographs these precipitates are visible as small pyramids (see Fig. 1) and show a polarization inversion of GaN in their core.[7–10] (2) The removal of hydrogen is often incomplete and significant amounts may remain after the activation (up to 20% of the Mg concentration).[11]

(3) Other defects, notably nitrogen vacancies in various charge states V_N^+/V_N^{3+}, may compensate the activated Mg acceptor.[3,12] Theoretical calculations predict the latter compensating mechanism to become relevant for Mg concentrations above 10^{18} cm^{-3}.

Understanding and eventually controlling these effects may be the key to overcome present-day *p*-type doping limitations and improve the efficiency of high-power devices. On the other hand, light metal nitrides like Mg_3N_2 have recently attracted interest as reversible hydrogen-storage materials.[13–16] While reversible hydrogen storage involves a phase transformation into a different crystal phase (amides or even hydrides), there are no indications that this occurs within the inversion domain boundaries. This raises the question if hydrogen can otherwise be incorporated into the Mg_3N_2 inclusions. Unfortunately, crystalline Mg_3N_2 is scarcely treated in literature. Beside the crystal structure most of the fundamental properties are unknown. In order to address the question of hydrogen in Mg_3N_2, the formation energies of interstitial and substitutional hydrogen, as well as of intrinsic point defects in Mg_3N_2 are needed. The purpose of this study is to close this gap by means of density functional theory (DFT) calculations. As the structure of the inversion domain boundaries is not fully resolved,[7–10] we focus on the natural bulk phase, which crystallizes in the antibixbyite structure.[17,18] It will be shown that these calculations provide important insight into chemical trends and can be used to estimate the interaction of hydrogen with Mg_3N_2 inclusions in GaN under growth conditions.

The remainder of this paper is organized as follows. In Sec. II, we will briefly summarize our theoretical approach. We will discuss the antibixbyite bulk structure in Sec. III A and then continue with intrinsic and hydrogen-related defects in Secs. III B and III C, respectively. Hydrogen in vacancies is considered in Sec. III D. Section IV is devoted to the consequences for GaN growth.

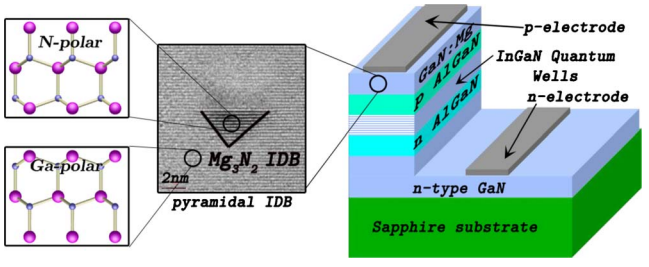

FIG. 1. (Color online) Conceptual design of an LED and the parasitic inversion domains appearing in the *p*-conductive part of the device at high Mg concentrations

II. METHODOLOGY

A. Computational details

The calculations are performed using DFT in the generalized-gradient approximation (GGA-PBE functional[19]) as implemented in the multiscale library S/PHI/nX.[20] The DFT implementation employs a plane-wave basis set and assumes periodic boundary conditions. Defects are therefore modeled in the supercell approach. The electron-ion interaction is described with norm-conserving pseudopotentials, which are generated[21] using the FHIPP98 program.[22] A plane-wave energy cutoff of 680 eV and a $2\times2\times2$ Monkhorst-Pack **k**-point sampling[23] ensures convergence in energy to within 1 meV, in the lattice constant to within 0.01 Å, and in

the bulk modulus to within 1 GPa. The DFT calculations yield formation energies of a defect X in charge-state q (Refs. 3 and 24)

$$E^f_{Xq} = E_{\text{tot}}[\text{Mg}_3\text{N}_2{:}X^q] - E_{\text{tot}}[\text{Mg}_3\text{N}_2] - \sum_i n_i\mu_i + q(E_{\text{Fermi}} + E_{\text{VBM}}) + E_{\text{align}}[q]. \quad (1)$$

$E_{\text{tot}}[\text{Mg}_3\text{N}_2{:}X^q]$ and $E_{\text{tot}}[\text{Mg}_3\text{N}_2]$ are the total energy of the defect cell and the bulk cell calculation, respectively. n_i denotes the number of additional atoms of species i (for vacancies n_i becomes negative) and μ_i denotes the corresponding chemical potential. The values in Sec. III are referred to a system in equilibrium with bulk Mg, Mg_3N_2, and H_2 molecule at $T=0$ K, which uniquely defines the chemical potentials. For charged systems, the chemical potential of the electrons is the Fermi energy, which in this paper is always referenced to the energy of the Mg_3N_2 valence-band maximum (VBM).

The supercell approach for defect introduces artificial interactions due to electrostatic interactions, wave-function overlap, and strain.[3,25] The artificial electrostatic interaction between a point defect and its periodic images is a dominant one. The energy contribution $E_{\text{align}}[q]$ in Eq. (1) is an energy correction for charged defects.[24] This correction cancels the interaction of the defect with its periodic images in the supercell approach and aligns the electrostatic potential to the bulk material. Using the correction allows to extract the isolated-defect limit already from modest supercell sizes. In this work we consider the 40 atoms body-centered-cubic (bcc) primitive cell and the 80 atoms simple cubic (sc) supercell of bulk Mg_3N_2. For the intrinsic point defects we will demonstrate that reasonable convergence in formation energy can then already achieved when using the 40-atoms cell. Another error source is hindered relaxations, i.e., elastic effects due to strain fields. They always enlarge the formation energies. A comparison of the structural properties of the defect cells indicates, that this error source plays a minor role in our calculations. The last critical error arises from the overlap of the defect states. This error is largest for extended states, i.e., when the defect state is energetically close to the valence bands or the conduction bands. It can be minimized by employing constant occupations of defect states throughout the Brillouin zone.[3] The remaining error has no specific direction and can therefore influence the formation energy in both ways.

The Fermi level in Eq. (1) appears as a free parameter. However, it is implicitly defined by the requirement of charge neutrality

$$\sum_{X^q} qc_{Xq} + c_h - c_e = 0 \quad (2)$$

for the total ensemble of defects and charge carriers. In thermodynamic equilibrium the concentration c_{Xq} of a defect X in charge state q is given by the Boltzmann distribution

$$c_{Xq} = N_0 N_{\text{conf}} \exp\left(\frac{E^f_{Xq}(E_{\text{Fermi}})}{k_bT}\right). \quad (3)$$

N_0 and N_{conf} denote the number of possible defect positions and the number of configurations within one position, respectively. k_bT is the thermal energy at the temperature T. The concentrations of the free charge carriers in a parabolic band are given[26] by

$$c_e = 2\left(\frac{m^*_e k_b T}{2\pi\hbar^2}\right)^{3/2} e^{(E_{\text{Fermi}}-E_{\text{CBM}})/k_bT}, \quad (4)$$

$$c_h = 2\left(\frac{m^*_h k_b T}{2\pi\hbar^2}\right)^{3/2} e^{(E_{\text{VBM}}-E_{\text{Fermi}})/k_bT}, \quad (5)$$

where m^* denotes the effective mass for the electrons or the holes, respectively. The solution of Eqs. (2)–(5) yields the concentrations of the specified defects and the position of the Fermi level. For a given set of chemical potentials μ_i, we solve these equations by a bisection method.

For Eqs. (4) and (5) the effective masses of electrons and holes are required. Unfortunately, experimental data are not available. In principle, the effective mass can be obtained from calculated band structures, but in the case of Mg_3N_2 these standard approaches fail due to the specific band structure, which is extremely flat near the VBM. We note that Eqs. (4) and (5) can be used even in this case if m^*_h is chosen according to the method outlined in the following.

B. Effective-mass calculation for flat bands

Using the definition of the effective mass m^*

$$\frac{1}{m^*} = \frac{1}{\hbar^2}\frac{d^2\epsilon(\mathbf{k})}{d\mathbf{k}^2}, \quad (6)$$

where $\epsilon(\mathbf{k})$ denotes the band dispersion, its value is easily obtained by fitting a parabola to the band structure. However, one often has to deal with a multitude of flat bands—especially near the VBM—where the attempt to fit individual bands yields an incorrect density of states (DOS). In the following we propose a scheme that avoids the fitting procedure and allows to obtain the effective masses directly from the calculated DOS.

The number of particles N is given by folding the density of states D with a distribution function f

$$N(E_{\text{Fermi}}) = \int_{-\infty}^{\infty} f(E - E_{\text{Fermi}})D(E)dE. \quad (7)$$

For numerical convenience $D(E)$ is given by $\Sigma_{n,\mathbf{k}} w_{\mathbf{k}} \delta(E - \epsilon_{n\mathbf{k}})$ with $\epsilon_{n\mathbf{k}}$ as the eigenenergies of the system. Equation (7) then becomes

$$N(E_{\text{Fermi}}) = \sum_{n\mathbf{k}} w_{\mathbf{k}} f(\epsilon_{n\mathbf{k}} - E_{\text{Fermi}}). \quad (8)$$

In the following, we concentrate on the electron description, where the distribution function is given by the Fermi-Dirac function. For $\frac{E_{\text{CBM}}-E_{\text{Fermi}}}{k_bT} \gg 1$ the Fermi-Dirac function can be

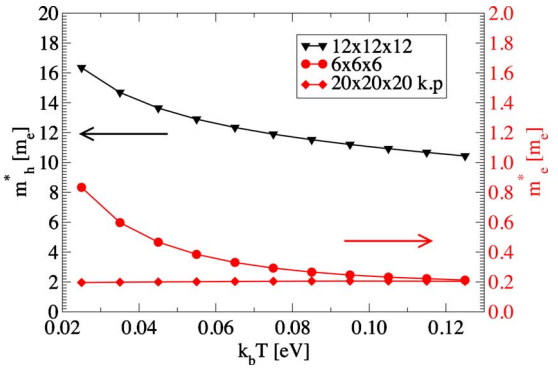

FIG. 2. (Color online) Effective hole and electron masses in Mg_3N_2 in dependence of the thermal energy. Note that the left-hand scale applies for hole mass and the right-hand scale for the electron mass.

approximated by the Boltzmann function. Further we assume that excitations are mainly driven by defect electrons, so that the number of valence electrons N_V is a constant. This is ensured when the condition $E_{\mathrm{Fermi}}-E_{\mathrm{VBM}} \gg E_{\mathrm{CBM}}-E_{\mathrm{Fermi}}$ holds.

These two conditions together define a suitable range for the choice of the Fermi level in the following equations:

$$\frac{1}{2}(E_{\mathrm{VBM}}+E_{\mathrm{CBM}}) \ll E_{\mathrm{Fermi}} \ll E_{\mathrm{CBM}}-k_bT. \tag{9}$$

Also the value for the thermal energy k_bT is limited. On the one hand, k_bT must be small enough to fulfill Eq. (9). On the other hand a high temperature allows the usage of a coarse grid of **k** points in Eq. (8). We will address this point below.

Choosing E_{CBM} as zero energy, the number of conduction electrons $N_C=N(E_{\mathrm{Fermi}})-N_V$ is given by

$$N_C \approx e^{E_{\mathrm{Fermi}}/k_bT} \underbrace{\int_0^\infty e^{-\epsilon/k_bT} D(\epsilon) d\epsilon}_{D_{\mathrm{eff}}(k_bT)}. \tag{10}$$

For a free electron with effective mass m^* the effective DOS D_{eff} on the right-hand side of Eq. (10) can be analytically calculated to be

$$D_{\mathrm{eff}}(k_bT) = \frac{2}{h^3}(2\pi m^* k_bT)^{3/2}. \tag{11}$$

To calculate the effective mass, we write Eq. (10) in the linear form

$$\ln[D_{\mathrm{eff}}(k_bT)] = \ln[N_C(E^{\mathrm{Fermi}})] - \frac{E^{\mathrm{Fermi}}}{k_bT}. \tag{12}$$

The right-hand side of Eq. (12) can be numerically calculated using Eq. (8). The effective mass is then easily obtained by combining Eqs. (11) and (12).

Figure 2 shows the convergence of the effective mass with increasing thermal energy. The quality of the effective mass depends strongly of the quality of the underlying density of states. The representation of the DOS by δ peaks introduces artifacts if the peak separation is comparable to (or even larger than) k_bT. This can be cured by increasing the temperature or the **k**-point sampling. For the electrons, we see this behavior when increasing the **k**-point sampling from a $6\times6\times6$ **k**-point mesh to a $20\times20\times20$ **k**-point mesh by a $\mathbf{k}\cdot\mathbf{p}$ interpolation.[27] For the holes, we find a fast convergence with respect to the **k**-point sampling; increasing the mesh resolution beyond a $12\times12\times12$ **k** -point mesh results in negligible changes in the hole mass. This is due to the nearly dispersion-free valence states near the VBM. The strong temperature dependence, visible in Fig. 2, is a consequence of the attempt to approximate the true DOS by an effective square-root function of the free-hole model.[28] For practical purposes, we choose m_h^* at the temperature of interest which correctly reproduces $D_{\mathrm{eff}}(T)$.

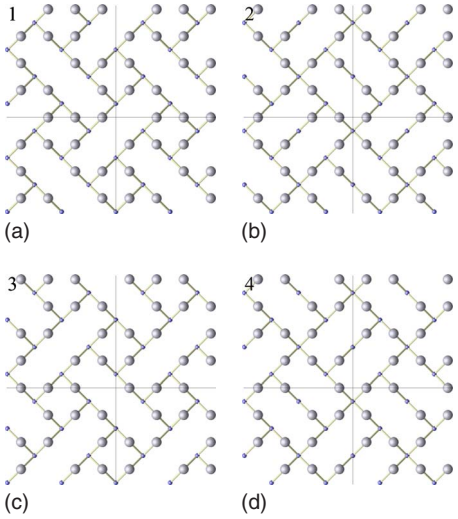

FIG. 3. (Color online) Geometry of the ideal (unrelaxed) Mg_3N_2 structure divided into the four atomic layers forming the cell. The small spheres refer the positions of the N atoms while the larger ones show the Mg atoms. The single slabs have been extended twice in the (100) and the (010) directions to give a better insight in the structure and the symmetry.

III. RESULTS

A. Bulk Mg_2N_2

Magnesium nitride is known to crystallize in the antibixbyite structure.[17,29] In order to introduce the structural motifs that are relevant for the point defects discussed below, we will describe the atomic structure of the bulk material first, following a similar scheme as Mokhtari and Akbarzadeh.[18] Starting from a hypothetical Mg_2N in the CaF_2 structure we obtain an idealized antibixbyite structure by removing 1/4 of all Mg atoms from a $2\times2\times2$ supercell. These *structural vacancies* are distributed equally such that every nitrogen atom ends up with six nearest neighbors. The resulting brick-like structure is shown in Fig. 3. For clarity the sc structure is divided into four slabs containing one nitrogen and one magnesium layer. Slab 1 and slab 3, as well as slab 2 and slab 4 are equivalent up to a lateral shift in the (110) direction. Thus, it is possible to reduce the 80-atoms sc cell to a 40 atoms primitive bcc cell.

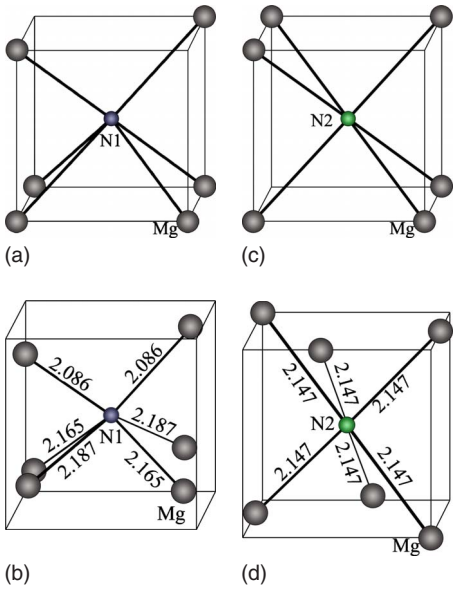

FIG. 4. (Color online) Visualization of the two inequivalent sites for nitrogen (N1 and N2). In the CaF_2 structure, the two inequivalent sites correspond to cubes with six Mg atoms on the edges and magnesium vacancies (a) on a face diagonal or (c) on the space diagonal. The corresponding relaxed configurations are given in figures (b) and (d), respectively.

Due to the presence of the structural vacancies the chemical surrounding of the nitrogen atoms is no longer identical. There are two inequivalent types of nitrogen atoms which differ in the arrangement of the Mg atoms (see Fig. 4). For the atoms labeled N1, the structural vacancies lie on a face diagonal, while they are on a space diagonal for N2 atoms. The 80-atom structure contains 24 N1 atoms and eight N2 atoms. In contrast to the N atoms, all Mg atoms have an identical chemical surrounding, consisting of a nearest-neighbor shell of three N1 and one N2.

Using this structure we performed DFT calculations for different volumes, allowing ionic relaxation. The fully relaxed antibixbyite structure is shown in Fig. 5. The calculated parameters are listed in comparison with theoretical and experimental data in Table I. The equilibrium lattice constant a_0, the bulk modulus B_0, and its pressure derivative B_0' were determined by fitting the energy-volume curve to the Murnaghan equation of state.[31] The atomic structure data included in Table I was obtained by x-ray diffraction[17] and the

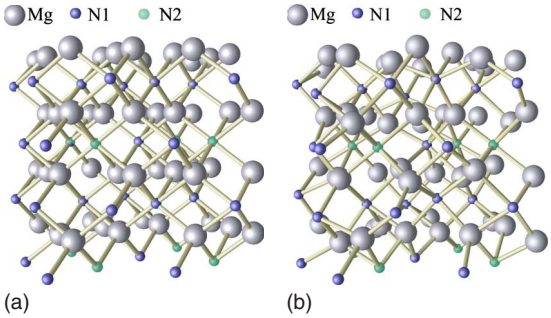

FIG. 5. (Color online) Ball and stick model of the ideal (left) and the relaxed (right) Mg_3N_2 structure.

TABLE I. Comparison of structural, elastic, and electronic parameters of bulk Mg_3N_2 with available theoretical and experimental data.

	This work	FP-LAPW (Ref. 18)	Expt. (Refs. 17 and 30)
a_{lat} (Å)	9.977	10.037	9.9528
B_0 (GPa)	108	110	
B_0'	3.76	4.02	
Band gap (eV)	1.59(Γ-Γ)	1.56(Γ-Γ)	3.15 (direct)
			2.85 (indirect)
Distance (Å)			
Mg-N1 (2x)	2.09	2.10	2.084
Mg-N1 (2x)	2.17	2.18	2.160
Mg-N1 (2x)	2.19	2.20	2.179
Mg-N2 (6x)	2.15	2.16	2.145
Int. coordinates			
v	0.969	0.969	0.9784
x	0.389	0.389	0.3890
y	0.153	0.153	0.1520
z	0.382	0.383	0.3823

optical band gap by reflection methods.[30] Our results are in good agreement with the available data, except the band gap, which shows the usual underestimation by semilocal exchange-correlation functionals such as GGA.

Performing the atomic relaxation, the initial nitrogen cubes become distorted, as shown in Fig. 4. The N1 atom ends up in a C_2 substructure with three different Mg-N1 bond lengths. The Mg-N2 distances are all equal and the substructure has the higher D_{3d} symmetry. The calculated distances are in good agreement with other theoretical and experimental work (Table I). In general the bonding distances are larger than the sum of the covalent atomic radii of Mg and N which is 2.05 Å. This is due to the fact that the coordination for magnesium and nitrogen is twice as high as the number of valence electrons. Thus, in a two-center bonding picture, each bonding orbital is occupied with only a single electron. This results in weaker chemical bonds (partially compensated by the electrostatic attraction between the ions[32]) with bond lengths slightly larger than in covalent bonds. The bonds are stretched by about 1.8–6.7 %.

In addition to the structural vacancies the structure exhibits a void (Fig. 6) in the center of a distorted octahedral substructure. This substructure consists of six Mg atoms with its center lying on the connection line between two N2 atoms. As will be shown in the next section, both the structural vacancies and the void are preferred sites for interstitials.

B. Intrinsic defects in magnesium nitride

We now turn to the discussion of point defects. In a first part we focus on native defects. Specifically, we consider the following defects. The Mg vacancy, the Mg interstitial at the position of the structural vacancy, the N1/N2 vacancies, and the N1/N2 split interstitials. Geometric details of the relaxed

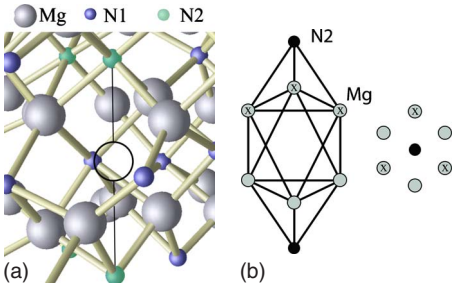

FIG. 6. (Color online) The DOH in Mg_3N_2, located in middle of the connection line between two N2 atoms. The right sketch shows the antiprismatic Mg cage.

structures are given in Table II for the vacancies and in Table III for the interstitials. Table IV lists the corresponding formation energies. The formation energies are given as calculated and corrected. For the most defects the agreement of the primitive 40-atoms cell and the 80-atoms cell are within 0.1 eV. For all vacancies we observe a relaxation of the surrounding atoms away from the defect center. The distance between the vacancy and its nearest neighbor increases by 0.06–0.19 Å (3–9 %) compared to the defect-free system. The reason for this is the decrease in the coordination number and therefore an increase in the number of electrons per two-center bond. This enhances the covalent part of the bonding (the ionic part of the bonding is also strengthened due to the shorter distance[32])

Our results show further that the nitrogen interstitial forms a N_2 complex in the crystal. Independent of the nitrogen type, the N-N bonding distance varies from 1.57 Å when negatively charged to 1.30 Å when positively charged. The bonding distance is noticeably stretched compared to similar chemical surroundings like hydrazine ($[N\text{-}N]^{4-}$, 1.45 Å) or diazine ($[N\text{-}N]^{2-}$, 1.24 Å). The formation energy differs for the two nitrogen sites and is more favorable for the N2-interstitial than for the N1 interstitial. The reason for this is that the N2 interstitial fits well in the N2 surrounding as indicated by the absence of structural changes in the environment. The N1 interstitial, on the other hand, severely distorts the local environment.

The magnesium interstitial forms four bonds to the neighboring nitrogen atoms. Three of these bonds have nearly the same distance, which is comparable to the smallest distance of a N1-Mg bond. The fourth bond length is very sensitive to the charge state. In case of the +2 state the bonding distance becomes minimal. The magnesium interstitial is then in the same charge state as the surrounding bulk magnesium atoms and fits well into the lattice.

TABLE II. Mg-V_N distances of the N1/N2 vacancy in charge state +1 and V_{Mg}-N distances of the Mg vacancy in charge state −2. The percentage values are with respect to the bulk material. (*N*x) gives the number of equivalent bonds.

	Distance (Å)		Distance (Å)
Mg-V_{N1} (2x)	2.15(+2.9%)	V_{Mg}-N1 (2x)	2.28(+9.1%)
Mg-V_{N1} (2x)	2.29(+5.8%)	V_{Mg}-N1 (2x)	2.35(+8.6%)
Mg-V_{N1} (2x)	2.32(+6.2%)	V_{Mg}-N1 (2x)	2.38(+9.0%)
Mg-V_{N2} (6x)	2.27(+5.9%)	V_{Mg}-N2 (6x)	2.33(+8.4%)

TABLE III. N-Mg distances of the N1/N2 interstitial and the Mg interstitial for different charge states. The number in brackets gives the number of equivalent bonds. The "*" denotes Mg atoms in the N1 interstitial calculation which are close enough to both nitrogen atoms that a bond to both is expected.

	$I_{N1/N2}$ distance (Å)		
Charge state	−1	0	+1
Mg-N1 (2x)	1.95	1.99	2.04
Mg-N1 (2x*)	2.05	2.08	2.12
Mg-N1 (2x*)	2.11	2.21	2.32
Mg-N1 (2x)	2.17	2.22	2.28
N1-N1	1.576	1.409	1.301
Mg-N2 (6x)	2.00	2.07	2.15
N2-N2	1.58	1.41	1.30
	I_{Mg} distance (Å)		
Charge state	0	+1	+2
Mg-N (3x)	2.09	2.09	2.09
Mg-N	2.17	2.16	2.16

C. Hydrogen in bulk magnesium nitride

After discussing the intrinsic point defects, we consider the incorporation of hydrogen into the bulk material next. We studied hydrogen in a variety of positions including bond-center sites, antibonding sites (see Fig. 7), the center position of the distorted octahedral hole (DOH), and the Mg structural vacancy. For a positively charged hydrogen defect (H^+) our calculations show that the antibonding position is the energetically most stable configuration. The formation energy between the two nitrogen types differs by ≈0.1 eV. The N-H distance (see Table V) is characteristic of a covalent N-H bond such as found, e.g., in hydrazine ($d_{N\text{-}H}$ = 1.03 Å).

For the negatively charged hydrogen defect (H^-) the DOH position becomes energetically most favorable. The distances between the hydrogen ion and its neighboring magnesium atoms range between 1.96 and 2.52 Å. The bond-center sites were found to be unstable and return to an antibonding site without a barrier. Also the structural vacancy position is not stable and relaxes into the antibonding site or the DOH position, depending on the charge state.

The stable hydrogen configurations agree well with the set of hydrogen adsorption sites which have been found for other nitrides.[2,4–6]

D. Hydrogen-based defect complexes

As shown above, interstitial H prefers the formation of an amidelike [N-H] complex when in positive or neutral charge

TABLE IV. Defect formation energies for all native defects as obtained from the supercell calculation (DFT) and including the supercell correction according to Ref. 24 (E_{align}).

	Formation energy (eV)			
	bcc-cell 40 atoms		sc-cell 80 atoms	
Defect	DFT	$+E_{\text{align}}$	DFT	$+E_{\text{align}}$
V_{Mg}				
−2	4.61	6.11	4.97	6.33
−1	4.63	5.16	4.85	5.27
0	4.85	4.85	4.88	4.88
I_{Mg}				
0	4.18	4.18	3.84	3.84
+1	1.13	1.48	1.26	1.63
+2	−1.74	−0.33	−1.35	−0.07
V_{N1}				
−1	5.17	5.60	4.99	5.24
0	2.41	2.41	2.49	2.49
+1	−0.08	0.08	−0.03	0.14
+2	−0.75	0.16	−0.60	0.20
+3	−1.49	0.70	−1.17	0.70
V_{N2}				
−1	4.88	5.26	4.96	5.24
0	2.46	2.46	2.45	2.45
+1	−0.09	0.09	−0.04	0.16
+2	−0.89	0.03	−0.72	0.23
+3	−1.89	0.33	−1.52	0.69
I_{N1}				
−1	5.76	6.09	5.82	6.01
0	4.39	4.39	4.44	4.44
+1	3.29	3.78	3.41	3.68
I_{N2}				
−1	5.04	5.35	5.08	5.31
0	3.91	3.91	3.96	3.96
+1	2.96	3.36	3.10	3.39

state and occupies the DOH when in negative charge state. Similar chemical surroundings can be provided by the Mg vacancy and the N vacancy. The N vacancy is comparable to the DOH: a void with a surrounding Mg cage. The free volume created by a nitrogen vacancy provides space for only a single-hydrogen atom. The Mg vacancy has significantly larger space and provides four bonding positions to create [N-H] complexes. The incorporation of hydrogen inside

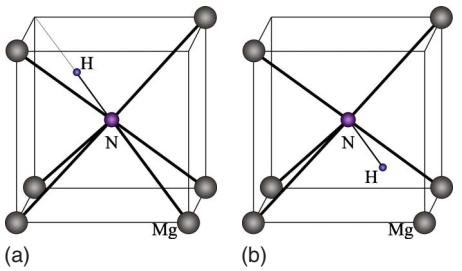

FIG. 7. (Color online) Hydrogen position for an antibonding site (left) and a bond-center site (right).

TABLE V. Distances of the hydrogen at antibonding nitrogen position in charge state +1.

	Distance (Å)		Distance (Å)
Mg-N1	2.14		
Mg-N1	2.16	Mg-N2 (3x)	2.24
Mg-N1	2.26		
Mg-N1	2.29		
Mg-N1	2.34	Mg-N2 (3x)	2.30
Mg-N1	2.39		
N1-H	1.05	N2-H	1.04

TABLE VI. Bond length in hydrogen-vacancy complexes.

V_N-H complex		V_{Mg}-H complex				
	Distance (Å)		[N-H] distance (Å)			
Mg-H (2x)	2.10	$[V_{Mg}$-H]		1.04		
Mg-H (2x)	2.46	$[V_{Mg}$-2H]		1.03		1.03
Mg-H (2x)	2.48	$[V_{Mg}$-3H]	1.04		1.04	1.04
Mg-H (6x)	2.364	$[V_{Mg}$-4H]	1.03	1.03	1.03	1.03

these vacancies gives therefore promising adsorption sites and is discussed now.

The structural details and the formation energies of the hydrogen-vacancy complexes are listed in Tables VI and VII, respectively. The hydrogen incorporation in the Mg vacancy results in strongly bound [N-H] complexes. Defining the binding energy via

$$E^f_{[V_{Mg}+nH]^{n-2}} + E^b = E^f_{V^{-2}_{Mg}} + nE^f_{H^+_{N2}}, \tag{13}$$

we found for the first incorporated hydrogen a binding energy of 2.35 eV. Further hydrogen is bound by 1.33 eV, 0.82 eV, and 0.02 eV, respectively. Especially the high binding energy of the first hydrogen enhances the formation of Mg vacancies in a hydrogen atmosphere. The $[V_N+H]$ defect complex provides only a binding energy of 0.33 eV in its most stable +2 charge state.

IV. DISCUSSION

A. Defect concentrations of bulk Mg_3N_2

In the previous section we have established the properties of defects in bulk Mg_3N_2 under arbitrarily chosen reference conditions (bulk Mg, Mg_3N_2, and H_2 for $T=0$ K). We will now consider realistic conditions by adjusting the chemical potentials to reflect actual GaN growth conditions.[11] The N chemical potential is set in equilibrium with GaN via

$$\mu_N + \mu_{Ga} = \mu_{GaN,bulk} \tag{14}$$

and the Mg chemical potential accordingly via

$$3\mu_{Mg} + 2\mu_N = \mu_{Mg_3N_2,bulk}. \tag{15}$$

The H chemical potential is then obtained from

$$2\mu_H = \mu_{H_2,\ T=0} + k_bT \ln\left(\frac{pV_q}{k_bT}\right) - k_bT \ln\left(\frac{k_bT}{2\Theta}\right). \tag{16}$$

V_q denotes hereby the phase-space volume

$$V_q = \left(\frac{2\pi\hbar^2}{m_H k_b T}\right)^{3/2}. \tag{17}$$

The rotational constant Θ for hydrogen is[33] 59.339 cm^{-1}. Corresponding characteristic conditions for GaN growth are Ga-rich conditions at ($\mu_{Ga}=\mu_{Ga(bulk)}$) at $T=1275$ K. Under metal-organic vapor-phase epitaxy conditions the sample is grown in presence of a hydrogen atmosphere. We therefore assume an equilibrium of the GaN sample with H_2 gas at a pressure of 1 bar. This value represents an upper limit to pressures commonly employed in experiment.

Figure 8 shows the formation energies of the native defects as function of the Fermi energy for this set of potentials. Over a wide range the most relevant defects are N and Mg vacancies. Only at extreme *p*-type conditions ($E_{Fermi}<0.3$ eV), the Mg^{2+} interstitial becomes favorable. When including hydrogen (Fig. 9), the H^+ interstitials and the $[V_{Mg}+H]^-$ are the dominant defects. Only at very *n*-type conditions ($E_{Fermi}>2.5$ eV) the Mg vacancy is the dominant defect. Table VIII shows the calculated defect concentrations and Fermi energies for H-free and H-rich conditions. The effective valence and conduction band masses needed to enforce the charge-neutrality condition [Eq. (2)] have been computed employing the approach proposed in Sec. II B to be $0.2m_e$ for the electrons and $10.7m_e$ for the holes. In the absence of any hydrogen, the Fermi level lies 1.72 eV above the VBM. The dominating defect is the positively charged nitrogen vacancy. It is worth noting that the charge neutrality is not achieved with compensating defects, but with free charge carriers. Overall, the total equilibrium concentrations of defects/holes are below 10^{14} cm^{-3}. The presence of hydrogen increases the defect concentration of the magnesium vacancies by an order of magnitude to $\approx 10^{15}$ cm^{-3} due to the formation of $[V_{Mg}H]$ complexes. The Fermi level does not change at all. However, the total amount of hydrogen incorporated into Mg_3N_2 is very low compared to typical concentrations in *p*-GaN (up to 10^{20} cm^{-3}). The discrepancy becomes even more obvious by considering the H/Mg ratio. While the [MgH] complex in fully passivated *p*-GaN has a ratio of 1 (the experimental ratio ranges between 0.2–0.8), it is $\sim 10^{-8}$ in Mg_3N_2. We thus conclude that Mg contained in Mg_3N_2 precipitates is unable to trap a relevant amount of hydrogen.

B. Thermal annealing

SIMS measurements[11] in the *p*-type region of actual device structures show that the removal of hydrogen is often incomplete. To identify the mechanism that prevent H removal and thus a complete activation of the *p*-type region, we focus now on the H drive-out from Mg_3N_2.

The drive-out procedure can be simulated by decreasing the H chemical potential at fixed temperature and assuming that all defects are immobile at this temperature, e.g., the concentration of the native defects remains constant. For the

TABLE VII. Hydrogen-related defects in Mg_3N_2. The Formation energy is shown as calculated in the supercell (DFT) and including the supercell correction E_{align}.

	Formation energy (eV)	
	bcc-cell 40 atoms	
Defect	DFT	$+E_{align}$
H_{N1}		
−1	4.55	4.86
0	1.62	1.62
+1	−1.09	−0.74
H_{N2}		
−1	4.49	4.77
0	1.54	1.54
+1	−1.18	−0.81
H @ DOH		
−1	2.42	2.78
0	2.05	2.05
+1	1.49	1.84
H_2 @ DOH		
0	1.44	1.44
$[V_{Mg}+H]$		
−1	2.48	2.95
0	2.72	2.72
+1	2.95	3.11
$[V_{Mg}+2H]$		
0	0.81	0.81
+1	0.73	0.90
+2	1.05	2.08
$[V_{Mg}+3H]$		
+1	−1.04	−0.82
+2	−0.87	0.19
+3	−0.58	2.08
$[V_{Mg}+4H]$		
+1	−0.52	−0.21
+2	−3.01	−1.65
+3	−2.77	0.51
+4	−2.44	2.52
$[V_{N1}+H]$		
+1	0.41	0.59
+2	−1.96	−1.02
+3	−1.89	0.40
$[V_{N2}+H]$		
+1	0.37	0.57
+2	−2.06	−1.06
+3	−1.95	0.48

following we assume a temperature of 900 K (m_e=0.2 and m_h=10.7) that is characteristic for the rapid thermal annealing process, which is used to remove H. We further assume that the H atoms can move freely once they are released from their defect centers. The hydrogen concentration as function of the H_2 partial pressure (μ_H) is shown in Fig. 10. As can be seen the removal of H happens in two steps. First the amount of hydrogen decreases only slightly. This is due to the removal of hydrogen from the antibonding nitrogen position, the DOH and the reduction in the $[V_{Mg}+2H]$ complex to $[V_{Mg}+H]$. The single hydrogen inside the magnesium vacancies remains stable until the H partial pressure falls below a critical value of $\approx 10^{-8}$ bar.

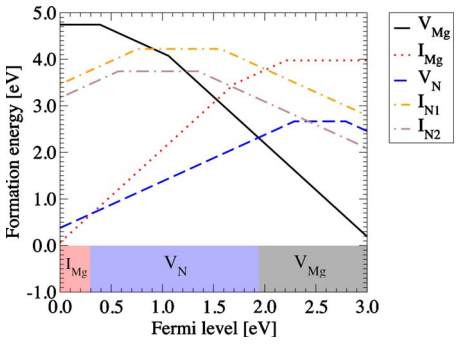

FIG. 8. (Color online) Formation energy of intrinsic defects as function of the Fermi level under GaN growth conditions (Ga rich, T=1275 K). Only charged states lowest in formation energy are shown. The colored regions at the bottom indicate which defect is energetically preferred.

This stability is caused by the large binding energy of 2.35 eV of the $[V_{Mg}+H]$ complex. An enlargement of the free carrier concentration ensures charge neutrality.

In conclusion, extreme conditions with respect to the H partial pressure and temperature are required to drive out hydrogen from the Mg_3N_2 phase. Thus, hydrogen incorporated during growth is strongly bound to Mg_3N_2 inclusions and will not be removed under realistic annealing conditions.

V. SUMMARY

We have identified the dominant native and hydrogen-induced point defects in magnesium nitride employing DFT calculations. Based on the calculated formation energies, we determined the equilibrium defect concentrations for Ga-rich growth conditions. In thermodynamic equilibrium the pure

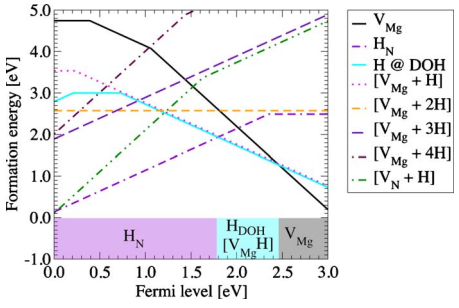

FIG. 9. (Color online) Formation energy of the energetically most favorable hydrogen-related point defects as function of the Fermi level. Identical growth conditions as in Fig. 8 are assumed. The colored regions at the bottom indicate the energetically preferred defect.

TABLE VIII. Point-defect concentrations, and the Fermi level without (left) and with (right) the presence of hydrogen at growth conditions specified in the text ($T=1275$ K, $p=1$ bar).

As grown		Grown in presence of hydrogen	
c_{V_N}	1.6×10^{14} cm^{-3}	c_{V_N}	1.7×10^{14} cm^{-3}
$c_{V_{Mg}}$	8.8×10^{11} cm^{-3}	$c_{V_{Mg}}$	1.7×10^{15} cm^{-3}
		c_H	3.6×10^{15} cm^{-3}
		$c_{V_{Mg}+H}$	1.7×10^{15} cm^{-3}
		$c_{V_{Mg}+2H}$	1.9×10^{13} cm^{-3}
Fermi level	1.74 eV	Fermi level	1.73 eV
Free carriers	$1.6\times10^{-14}e^+$	Free carriers	$1.6\times10^{-13}e^+$

single-crystalline material is found to be an essentially defect-free insulator. The nitrogen vacancy has the largest defect concentration with 2×10^{14} cm^{-3}. If grown in the presence of hydrogen, the formation of strongly bound [N-H] complexes is favorable. Isolated interstitial H atoms form singly coordinated strong bonds to N atoms when in a positive-charged state or occupies Mg vacancies in the negative-charge state. Maximum concentrations at realistic growth conditions are nevertheless small (only 4×10^{15} cm^{-3}), particularly when comparing with the concentration of hydrogen in [Mg-H] complexes in Mg:GaN ($\approx10^{18}$ cm^{-3}). The significantly lower solubility of H in Mg_3N_2 compared to GaN, together with the fact that the volume fraction of Mg_3N_2 in Mg-doped GaN is small, allows us to conclude that both, the H incorporation in Mg_3N_2 and the desorption of H from Mg_3N_2 will not affect the H distribution and the removal in actual devices.

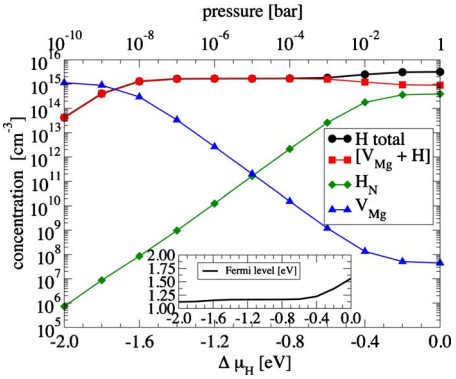

FIG. 10. (Color online) Calculated concentration of defects which play an important role in the thermal annealing as function of the applied chemical hydrogen potential at $T=900$ K. The corresponding H_2 partial pressure is displayed on the top axis. The inset shows the Fermi level as function of the chemical potential.

ACKNOWLEDGMENTS

We thank Norbert Linder, Martin Strassburg, and Martin Albrecht for stimulating and fruitful discussions. This work was financed by the German ministry of Education and Research, Project No. 03X0512G (VEKTRA).

[1] F. A. Ponce and D. P. Bour, Nature (London) **386**, 351 (1997).
[2] J. Neugebauer and C. G. Van de Walle, Appl. Phys. Lett. **68**, 1829 (1996).
[3] C. G. Van de Walle and J. Neugebauer, J. Appl. Phys. **95**, 3851 (2004).
[4] A. F. Wright, C. H. Seager, S. M. Myers, D. D. Koleske, and A. A. Allerman, J. Appl. Phys. **94**, 2311 (2003).
[5] A. F. Wright and S. M. Myers, J. Appl. Phys. **94**, 4918 (2003).
[6] W. R. Wampler and S. M. Myers, J. Appl. Phys. **94**, 5682 (2003).
[7] P. Vennéguès, M. Leroux, S. Dalmasso, M. Benaissa, P. De Mierry, P. Lorenzini, B. Damilano, B. Beaumont, J. Massies, and P. Gibart, Phys. Rev. B **68**, 235214 (2003).
[8] J. E. Northrup, Appl. Phys. Lett. **82**, 2278 (2003).
[9] P. Vennéguès, M. Benaissa, B. Beaumont, E. Feltin, P. D. Mierry, S. Dalmasso, M. Leroux, and P. Gibart, Appl. Phys. Lett. **77**, 880 (2000).
[10] M. Leroux, P. Vennéguès, S. Dalmasso, M. Benaissa, E. Feltin, P. D. Mierry, B. Beaumont, B. Damilano, N. Grandjean, and P. Gibart, Phys. Status Solidi A **192**, 394 (2002).
[11] N. Linder and M. Strassburg (private communication).
[12] S. M. Myers, A. F. Wright, M. Sanati, and S. K. Estreicher, J. Appl. Phys. **99**, 113506 (2006).
[13] Y. Kojima, Y. Kawai, and N. Ohba, J. Power Sources **159**, 81 (2006).
[14] Y. Nakamori, G. Kitahara, K. Miwa, and S. Towata, Appl. Phys. A: Mater. Sci. Process. **80**, 1 (2005).
[15] P. Chen, Z. Xiong, J. Luo, J. Lin, and K. L. Tan, Nature (London) **420**, 302 (2002).
[16] J. Lu, Z. Z. Fang, Y. J. Choi, and H. Y. Sohn, J. Phys. Chem. C **111**, 12129 (2007).
[17] D. E. Partin, D. J. Williams, and M. O'Keeffe, J. Solid State Chem. **132**, 56 (1997).
[18] A. Mokhtari and H. Akbarzadeh, Physica B **337**, 122 (2003).
[19] J. P. Perdew, K. Burke, and M. Ernzerhof, Phys. Rev. Lett. **77**, 3865 (1996).
[20] S. Boeck, C. Freysoldt, A. Dick, L. Ismer, and J. Neugebauer (unpublished).
[21] For our pseudopotentials we used as cut-off radii ($r_s^{cut}, r_p^{cut}, r_d^{cut}, r_f^{cut}$) in atomic units: N $2s^2p^3d^0$ (1.5,1.5,1.5) Troullier-Martin type, Mg $3s^3p^03d^0$ (1.2,1.6,1.5) Haman type, and H $1s^12p^03d^04f^0$ (1.276,1.276,0.350,1.276) Troullier-Martin type.
[22] M. Fuchs and M. Scheffler, Comput. Phys. Commun. **119**, 67 (1999).
[23] H. J. Monkhorst and J. D. Pack, Phys. Rev. B **13**, 5188 (1976).
[24] C. Freysoldt, J. Neugebauer, and C. G. Van de Walle, Phys. Rev. Lett. **102**, 016402 (2009).
[25] C. W. M. Castleton, A. Höglund, and S. Mirbt, Modell. Simul. Mater. Sci. Eng. **17**, 084003 (2009).

[26] C. Kittel, *Einführung in die Festkörperphysik*, 14th ed. (Oldenburg Verlag, München, Wien, 2006).
[27] C. Persson and C. Ambrosh-Draxl, Comput. Phys. Commun. **177**, 280 (2007).
[28] In this specific case, $D(E)$ resembles a step function in the energy region of interest. Equation (10) then yields $D_{\text{eff}} \propto k_b T$. Comparison with Eq. (11) shows that $m_h^* \propto (k_b T)^{-1/3}$, as observed in Fig. 2.
[29] M. G. M. Armenta, A. Reyes-Serrato, and M. A. Borja, Phys. Rev. B **62**, 4890 (2000).
[30] K. Toyoura, T. Goto, K. Hachiya, and R. Hagiwara, Electrochim. Acta **51**, 56 (2005).
[31] F. D. Murnaghan, Proc. Natl. Acad. Sci. U.S.A. **30**, 244 (1944).
[32] A. Costales, M. A. Blanco, A. Martin Pendas, A. K. Kandalam, and R. Pandey, J. Am. Chem. Soc. **124**, 4116 (2002).
[33] B. P. Stoicheff, Can. J. Phys. **35**, 730 (1957).